

Article

Synergistic Effect in Plasmonic CuAu Alloys as Co-Catalyst on SnIn₄S₈ for Boosted Solar-Driven CO₂ Reduction

Zhengrui Yang¹, Jinman Yang¹, Kefen Yang¹, Xingwang Zhu² , Kang Zhong¹, Ming Zhang¹ , Haiyan Ji¹, Minqiang He¹, Huaming Li¹ and Hui Xu^{1,*}

¹ School of Materials Science & Engineering, Institute of Energy Research, Jiangsu University, Zhenjiang 212013, China

² School of Environmental and Chemical Engineering, Yangzhou University, Yangzhou 225009, China

* Correspondence: xh@ujs.edu.cn

Abstract: The photoreduction of CO₂ to chemical fuels represents a promising technology to mitigate the current energy dilemma and global warming problems. Unfortunately, the original photocatalysts suffer from many side reactions and a poor CO₂ conversion efficiency. The rational combination of active co-catalyst with pristine photocatalysts for promoting the adsorption and activation of CO₂ is of vital importance to tackle this grand challenge. Herein, we rationally designed a SnIn₄S₈ nanosheet photocatalyst simultaneously equipped with CuAu alloys. The experimental results proved that the CuAu alloy can trap the electrons and enhance the separation and transport efficiency of the photogenerated carrier in the photocatalyst, alleviating the kinetical difficulty of the charge transfer process because of the preferable localized surface plasmon resonance (LSPR). Furthermore, the CuAu alloy works as the synergistic site to increase the CO₂ adsorption and activation capacity. The optimized CuAu-SnIn₄S₈ photocatalyst exhibited a superior performance with CO generation rates of 27.87 μmol g⁻¹ h⁻¹ and CH₄ of 7.21 μmol g⁻¹ h⁻¹, which are about 7.6 and 2.5 folds compared with SnIn₄S₈. This work highlights the critical role of alloy cocatalysts in boosting a CO₂ activation and an efficient CO₂ reduction, thus contributing to the development of more outstanding photocatalytic systems.

Keywords: SnIn₄S₈; CuAu alloy; synergistic effect; photocatalysis; CO₂ reduction



Citation: Yang, Z.; Yang, J.; Yang, K.; Zhu, X.; Zhong, K.; Zhang, M.; Ji, H.; He, M.; Li, H.; Xu, H. Synergistic Effect in Plasmonic CuAu Alloys as Co-Catalyst on SnIn₄S₈ for Boosted Solar-Driven CO₂ Reduction. *Catalysts* **2022**, *12*, 1588. <https://doi.org/10.3390/catal12121588>

Academic Editor: Jose L. Hueso

Received: 9 November 2022

Accepted: 25 November 2022

Published: 6 December 2022

Publisher's Note: MDPI stays neutral with regard to jurisdictional claims in published maps and institutional affiliations.



Copyright: © 2022 by the authors. Licensee MDPI, Basel, Switzerland. This article is an open access article distributed under the terms and conditions of the Creative Commons Attribution (CC BY) license (<https://creativecommons.org/licenses/by/4.0/>).

1. Introduction

As the scale of human activities continues to expand, global warming is known as an ever-increasingly severe global environmental problem [1]. In addition, the contradiction between the universal fast-growing energy demand and the global energy imbalance is growing acute [2]. The above problems have driven numerous researches for the sustainable transformation of CO₂ into hydrocarbons and highly valuable chemical products. Among the available resources, the renewable solar photocatalytic transformation of CO₂ via semi-conducting photocatalysts shows the most promising application in simultaneously solving renewable energy production and alleviating the warming effect [3,4]. However, the photocatalytic performance of single semiconductors is hindered by a serious electron-hole pairs recombination and the poor adsorption and activation capacities of inert CO₂ molecules on the surface [5,6]. From this perspective, rationally developing suitable photocatalysts appears to be particularly significant.

Among the various previously reported semiconductors photocatalysts, bimetallic sulfides have aroused great scientific interest due to their unique characteristics, for instance, their adjustable morphology, enriched active sites, controllable band structure and fast photoexcited charge dynamics [7,8]. Particularly, SnIn₄S₈ is a typical n-type bimetallic sulfide semiconductor with a cubic spinel structure [9]. Featured by the narrow band gap, easily adjustable electronic and optical properties, SnIn₄S₈ is a suitable candidate in high-energy batteries and photocatalytic applications [10,11]. The above advantages

inspire us to consider their potential roles in photocatalytic CO₂ reduction. However, the poor light utilization and short lifetime of photoinduced carriers seriously influence the photocatalytic ability in visible light. Therefore, SnIn₄S₈ needs to be modified to suppress fast recombination of photoinduced carriers and enhance the ability to absorb and activate CO₂ molecules [12].

Decorating cocatalysts on the photocatalyst surface represents one of the most appealing means to enhance the CO₂ photoreduction performance. On the one hand, cocatalysts can serve as electron sinks to capture photoexcited electrons, which accelerates the efficient charge separation and simultaneously restrains the occurrence of side reactions [13,14]. On the other hand, cocatalysts can act as extra active sites to lower the activation potentials of CO₂ molecules for the enhancement of the adsorption and activation of reactants, thus making for the enhanced CO₂ conversion efficiency [15,16]. Up to now, various metal cocatalysts like Pd, Au, Ag, Pt and Cu et al. have been developed to modify the semiconductor photocatalyst for a photocatalytic CO₂ conversion [17]. However, the function of single-metal cocatalysts has resulted in the low selectivity of carbon-based products and sluggish enhancements in the total amounts of products [18,19]. Previous studies have demonstrated that alloys composed of two or multiple metals have huge potential for optimizing the catalytic performance via providing different local atomic arrangements on the catalyst surface to tune the adsorption configuration of the reactants and CO₂ and control the d-band centers of the catalyst [20–22]. The synergistic effect between the various atoms of the alloy cocatalyst will offer coupled sites to stabilize the CO₂ molecules and accurately adjust the adsorption and desorption of crucial reaction intermediates. Moreover, the Schottky barrier that appeared at the alloy/substrate interface can realize an efficient charge separation because of the internal electric field [23,24].

On account of the high activation potential barrier of CO₂ molecules, as well as multiple electrons and protons transfer and side reactions involved in the process of CO₂ reduction, it is anticipated that the reasonable design of alloy cocatalysts can play a synergy in terms of promoting the CO₂ activation and trapping the photogenerated charge [25]. Copper (Cu), widely recognized as a cocatalyst, facilitates the different forms of hydrocarbons for its strong binding capacity with CO₂ molecules and reaction substrates [26]. In the design of alloys, integrating Cu with noble metals (Ag, Pt and Au) is the most favorable approach, not only leading to an increase in visible light absorption but also in photoexcited electron-hole pairs separation owing to the superior localized surface plasmon resonance (LSPR) and charge storage properties [27–29]. Taken together, it is expected that the alloying of active metal Cu with plasmonic metal Au supplies an ideal platform to optimize the photoreduction performance in terms of modifying SnIn₄S₈ [30,31].

In this work, we introduced the CuAu alloy cocatalysts supported on the SnIn₄S₈ nanosheet photocatalyst for an optimized photocatalytic activity in the CO₂ reduction to CO and CH₄. The introduction of the CuAu alloy's nanoparticles drives the transfer of photoexcited electrons to the co-catalyst and improves the light absorption ability. Furthermore, the AuCu alloy can act as the synergistic site to boost CO₂ adsorption and activation. Among the designed samples, the Cu₁₀Au₁-SnIn₄S₈ achieved the activity of 27.87 μmol g⁻¹ h⁻¹ of CO and 7.21 μmol g⁻¹ h⁻¹ of CH₄, which are about 7.6 and 2.5 folds compared with SnIn₄S₈. This work offers a new approach for designing alloy cocatalysts-modified metal sulfides for the efficient photocatalytic conversion of CO₂ to fuels.

2. Results and Discussion

The synthetic process of the Cu_xAu_y-SnIn₄S₈ is distinctly displayed in Figure 1. Firstly, the morphologies of as-synthesized SnIn₄S₈ and Cu₁₀Au₁-SnIn₄S₈ were investigated by scanning electron microscopy (SEM) and transmission electron microscopy (TEM). As shown in Figure 2a, it is obvious that SnIn₄S₈, with a wavy-like morphology, was fabricated by means of a simple hydrothermal method. Furthermore, the TEM images further demonstrate the unique structure of the SnIn₄S₈ nanosheet, where the multiple thin sheets with wrinkles can be clearly observed (Figure 2b). The dispersed irregular nanosheets' structure

facilitates an increase in more exposed active sites on a high surface area and shortens the charge diffusion distance to inhibit their recombination [32]. As illustrated in Figure 2c, the CuAu alloy's nanocrystals are an in-situ growth on SnIn₄S₈ nanosheets by the method of aqueous solution synthesis. The microstructure of Cu₁₀Au₁-SnIn₄S₈ can be further exhibited by TEM images (Figure 2d–f). The morphology of SnIn₄S₈ remains unaltered after the loading of the CuAu alloy. The Cu₁₀Au₁ alloy's nanoparticles show a round-shaped form with a uniform particle diameter of about 8 nm, which are relatively even and supported on the surface of SnIn₄S₈. In the case of Cu₁₀Au₁-SnIn₄S₈, a high resolution TEM (HRTEM) image shows that the characteristic spacing is 0.32 nm, which belongs to the (311) plane of SnIn₄S₈ (Figure 2l). The CuAu alloy nanoparticle shows the lattice distances of 0.24 and 0.21 nm, respectively, corresponding with the (201) and (211) planes for the CuAu alloys, indicating that the CuAu alloys are successfully loaded on the surface of SnIn₄S₈. Elemental mapping images (Figure 2g–k) and Energy-Dispersive X-Ray spectroscopy (EDX) (Figure S1) were obtained to analyze the components of Cu₁₀Au₁-SnIn₄S₈. The distribution of the S, In and Sn elements greatly corresponds to the structure of SnIn₄S₈. In addition, Cu and Au elements are almost distributed at the same position in the selected area, confirming the successful formation of the CuAu alloy.

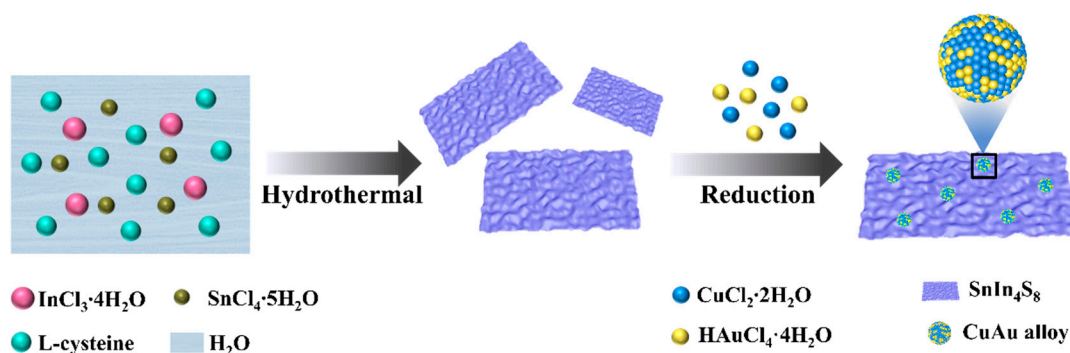


Figure 1. Schematic illustration for the synthetic process of Cu₁₀Au₁-SnIn₄S₈.

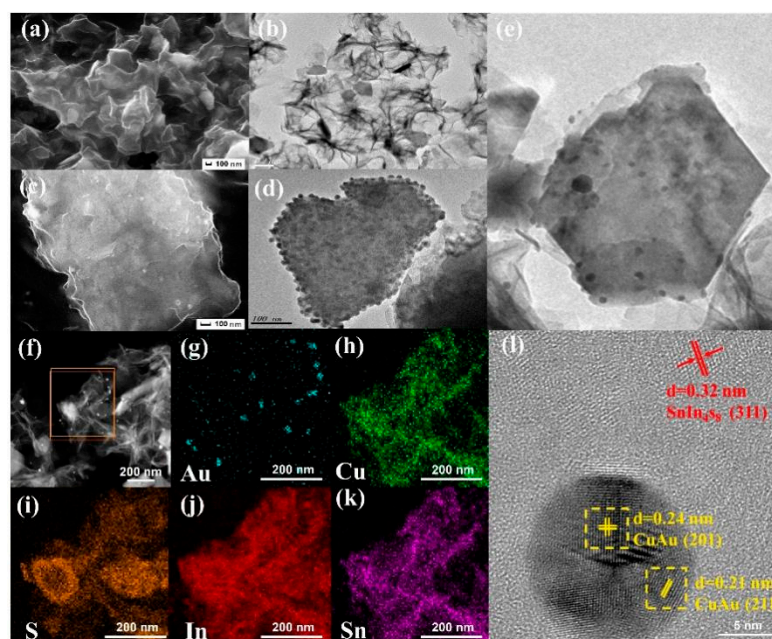


Figure 2. (a) SEM and (b) TEM images of SnIn₄S₈. (c) SEM and (d–f) TEM images of Cu₁₀Au₁-SnIn₄S₈. (g–k) Elemental mapping of Cu₁₀Au₁-SnIn₄S₈. (l) HRTEM image of Cu₁₀Au₁-SnIn₄S₈.

X-ray diffraction (XRD) was used to explore the crystal structures of the samples. As illustrated in Figure 3a, the diffraction peaks of SnIn_4S_8 are perfectly matched with the crystalline planes of cubic SnIn_4S_8 (JCPDS 42-1306), which demonstrate that SnIn_4S_8 was successfully synthesized. After the decoration of the Au nanoparticles on SnIn_4S_8 , the additional peaks at 38.1° , 44.3° , 64.5° and 77.5° in the XRD pattern for $\text{Au}_2\text{-SnIn}_4\text{S}_8$ correspond to the (100), (200), (220) and (311) planes of Au (JCPDs 04-0784), illustrating that the Au nanoparticles were successfully supported on the surface of SnIn_4S_8 . The diffraction peaks in the SnIn_4S_8 loaded with Cu at 43.2° , 50.4° and 74.1° can be indexed to (111), (200) and (220) planes of Cu (JCPDS 04-0836). Significantly, in the case of the XRD pattern of $\text{Cu}_{10}\text{Au}_1\text{-SnIn}_4\text{S}_8$, aside from the main typical peaks ascribing to SnIn_4S_8 , the other characteristic peaks are well assigned to the range of the XRD patterns from Au (JCPDs 04-0784) to Cu (JCPDs 04-0836) and can be clearly observed, which present a representative characteristic for the CuAu alloy [19,26].

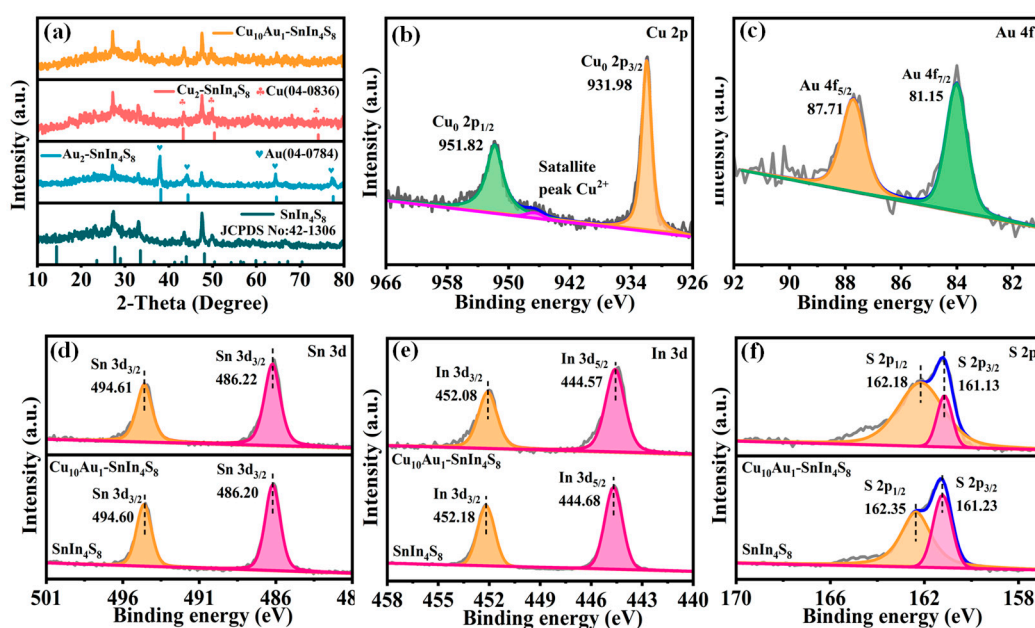


Figure 3. (a) XRD patterns of the as-prepared samples. XPS spectra for (b) Cu 2p and (c) Au 4f of $\text{Cu}_{10}\text{Au}_1\text{-SnIn}_4\text{S}_8$, (d) Sn 3d, (e) In 3d and (f) S 2p of SnIn_4S_8 and $\text{Cu}_{10}\text{Au}_1\text{-SnIn}_4\text{S}_8$.

The X-ray photoelectron spectra (XPS) further studied the chemical states of the elements and electronic states of photocatalysts. The existence of S, In and Sn, along with Cu and Au, were affirmed in the wide spectrum of both SnIn_4S_8 and $\text{Cu}_{10}\text{Au}_1\text{-SnIn}_4\text{S}_8$ (Figure S2), which agrees with accordingly elemental mapping images. As for the XPS spectra of bare SnIn_4S_8 , there are two typical peaks in the Sn 3d spectra at about 486.01 and 494.52 eV, belonging to Sn $3d_{5/2}$ and Sn $3d_{3/2}$, respectively (Figure 3d) [9]. The In 3d spectra in Figure 3e reveal that the binding energies at around 444.40 and 452.94 eV are arisen from the In $3d_{5/2}$ and In $3d_{3/2}$ peaks [10]. The S 2p spectra clearly exhibit the two diffraction peaks of S $2p_{3/2}$ and S $2p_{1/2}$ at the binding energy of 161.0 and 162.39 eV, respectively [11]. In addition, the additional peak positioned at 163.80 eV suggested the presence of Sn (IV)-S on the surface of the samples (Figure 3f) [5]. The Au 4f levels of the $\text{Cu}_{10}\text{Au}_1\text{-SnIn}_4\text{S}_8$ spectra at around 81.15 and 87.71 eV correspond to the Au $4f_{7/2}$ and Au $4f_{5/2}$, which can be attributed to Au^0 (Figure 3c) [21]. In regard to the Cu 2p spectra (Figure 3b), the binding energy at 931.98 and 951.82 eV are ascribed to Cu $2p_{3/2}$ and Cu $2p_{1/2}$, which is in the form of Cu^0 [15]. In addition, a satellite peak at 946.59 eV can be indexed to Cu (II) caused by the inevitable surface oxidation of metallic Cu [26]. These XPS results further demonstrate the formation of the CuAu alloys in the $\text{Cu}_{10}\text{Au}_1\text{-SnIn}_4\text{S}_8$. Notably, Sn 3d, In 3d and S 2p peaks shift to a higher binding energy by different values as compared to the pure

SnIn_4S_8 , indicating the charge transfer from SnIn_4S_8 to the CuAu alloy due to the difference in the Fermi levels [16]. This also suggests that there is an interface between the SnIn_4S_8 and AuCu alloy, which contributes to the transfer and migration of free electrons and the enhancement of the photocatalytic activity [33,34]. The phenomenon is also explored by the XPS valence band spectra (Figure S3), where the VBM of $\text{Cu}_{10}\text{Au}_1\text{-SnIn}_4\text{S}_8$ shifts towards a lower value compared with pure SnIn_4S_8 , respectively, further confirming the electron transport through the interface between SnIn_4S_8 and the AuCu alloy [35].

In order to verify the impacts of the modified CuAu alloy, the activity of the synthesized photocatalysts in a CO_2 reduction including triethanolamine (TEOA) as the sacrificial agent was investigated under a 300 W Xe lamp irradiation. There were no liquid-phase products detected, and the average evolution rates of gas-phase products by diverse CuAu alloys integrated on SnIn_4S_8 , monometallic $\text{Au}_2\text{-SnIn}_4\text{S}_8$ and $\text{Cu}_2\text{-SnIn}_4\text{S}_8$ and SnIn_4S_8 are compared in Figure 4a. The pristine SnIn_4S_8 catalyst generated relatively less CO , CH_4 and H_2 , which elucidates the generation rates for $3.6 \mu\text{mol g}^{-1} \text{h}^{-1}$, $2.5 \mu\text{mol g}^{-1} \text{h}^{-1}$ and $0.3 \mu\text{mol g}^{-1} \text{h}^{-1}$, respectively. With the integration of single metal nanocrystals on SnIn_4S_8 , photocatalytic production has been significantly improved. On the one hand, the introduced metal species with an excellent electron conduction capacity can effectively enrich electrons and provide additional active sites for the accelerating CO_2 reduction reaction [36]. Especially, gold nanoparticles (Au NPs) can generate large amounts of hot electrons with a high energy to reduce CO_2 into CO and CH_4 owing to the strong LSPR effect, and its electron storage properties lead to enhanced electron-hole pair separation in the structure of the metal-semiconductor composition [36,37]. On the other hand, the interfaces between the metal nanocrystals and SnIn_4S_8 can facilitate a charge transfer to accelerate the reaction kinetics [38]. Significantly, the CuAu alloy as the cocatalyst is demonstrated to be a very beneficial catalyst which shows the obviously improved activity compared with the single metal loaded on SnIn_4S_8 . Among the various amount of the CuAu alloy-loaded SnIn_4S_8 , $\text{Cu}_{10}\text{Au}_1\text{-SnIn}_4\text{S}_8$ displays the most outstanding photocatalytic performance with CO generation rates of $27.87 \mu\text{mol g}^{-1} \text{h}^{-1}$ and a CH_4 evolution rate of $7.21 \mu\text{mol g}^{-1} \text{h}^{-1}$, which are about 7.6 and 2.5 folds compared with SnIn_4S_8 , respectively. This result suggests that the synergistic function between the Cu and Au components in the CuAu alloys is indispensable for the photocatalytic activity improvement of CO and CH_4 . The formation rates of each product enhance with the larger Cu/Au molar ratio because of the additional active sites. Meanwhile, the latest photocatalysts for CO_2 reduction and their abilities are listed in Table S1. The performance of $\text{Cu}_{10}\text{Au}_1\text{-SnIn}_4\text{S}_8$ is in a competitive position. However, further, the increasing Cu/Au molar ratio results in a reduced photocatalytic performance, which can be attributed to the recombination centers generated by adjoining CuAu alloys on SnIn_4S_8 , making the immediate recombination of photoinduced carriers [39].

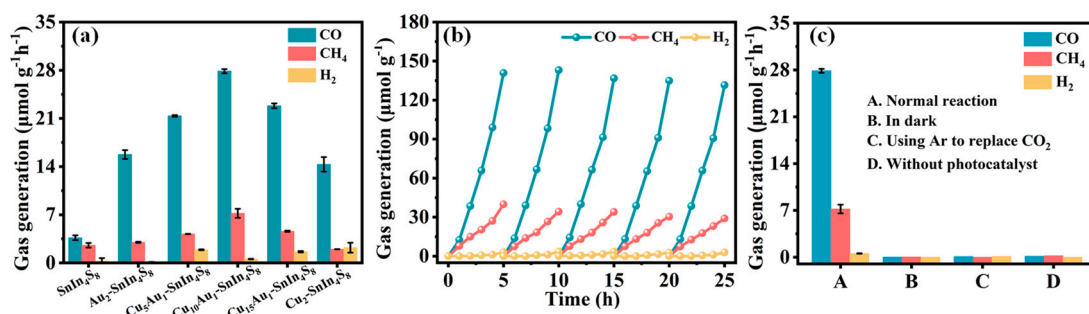


Figure 4. (a) CO , CH_4 and H_2 formation rates of the samples. (b) Long-time photocatalytic stability of $\text{Cu}_{10}\text{Au}_1\text{-SnIn}_4\text{S}_8$ for 25 h. (c) Comparison of photocatalytic CO_2 reduction performance in different conditions.

Apart from the excellent photocatalytic activity, the $\text{Cu}_{10}\text{Au}_1\text{-SnIn}_4\text{S}_8$ also exhibits outstanding photocatalytic stability. As presented in Figure 4b, $\text{Cu}_{10}\text{Au}_1\text{-SnIn}_4\text{S}_8$ still holds

great durability after 25 h with 5 recycling tests, illustrating that $\text{Cu}_{10}\text{Au}_1\text{-SnIn}_4\text{S}_8$ catalysts are suitable for a photocatalytic CO_2 reduction because of the well-maintained structure and shape. The XRD and SEM patterns of $\text{Cu}_{10}\text{Au}_1\text{-SnIn}_4\text{S}_8$ after long-term photocatalytic cycles have very little obvious change in the structure and morphology (Figures S4 and S5). In addition, the control experiments were carried out in the dark, in the Ar atmosphere and in the absence of photocatalysts (Figure 4c). There is nearly no product in the photocatalytic CO_2 reduction process, proving the fact that the carbon-containing products are actually triggered by the photocatalytic CO_2 reduction instead of adsorbed carbon species.

The photo absorption capacity of the as-obtained materials was investigated by the UV-vis diffuse reflectance spectrum (DRS). As shown in Figure 5a, SnIn_4S_8 displays a steep absorption region of about 650 nm in the visible light region owing to the narrow bandgap. After the loading of Au nanocrystals, the absorption edge of $\text{Au}_2\text{-SnIn}_4\text{S}_8$ does not appear as an extra absorption peak caused by the LSPR effect of the plasmonic metal. This can be illustrated by the fact that the dark yellow-green SnIn_4S_8 appears to have a strong absorption intensity and broad absorption range in the UV-vis region, which may cover up the plasmonic band of Au [16]. When the Cu and CuAu nanocrystals were introduced, the background absorption was significantly improved to the longer wavelength region, which greatly matches the color of the catalysts changing from dark yellow-green to black. Furthermore, the band gap (E_g) of the pure SnIn_4S_8 was calculated by a typical Tauc approach. As exhibited in Figure S6, the E_g of SnIn_4S_8 is estimated to be 1.92 eV, which is suitable for the process of a photocatalytic CO_2 reduction. In addition, the Mott-Schottky plots of SnIn_4S_8 were measured at 1500, 2000 and 2500 Hz, respectively, and the flat-band potential of SnIn_4S_8 is about -0.76 V (vs. NHE, pH = 7) (Figure S7). Generally speaking, the positive slope of the Mott-Schottky plot indicates that SnIn_4S_8 belongs to n-type semiconductors, whose flat-band position is nearly at the Fermi level [14,37]. As shown in green line in Figure S3, the gap between the Fermi level and the VB of SnIn_4S_8 is approximately 1.51 eV from the XPS valence band spectrum. Therefore, the VB value of SnIn_4S_8 was estimated to be 0.75 eV (vs. NHE, pH = 7). According to the following formula: $E_{\text{CB}} = E_{\text{VB}} - E_g$, the value of CB can be determined as -1.17 V (vs. NHE, pH = 7). In summary, the obtained band structure of photocatalyst conforms to the thermodynamic potential of a photocatalytic CO_2 reduction, and the photogenerated electrons in the CB of SnIn_4S_8 possess a negative potential enough for the photocatalytic CO_2 reduction.

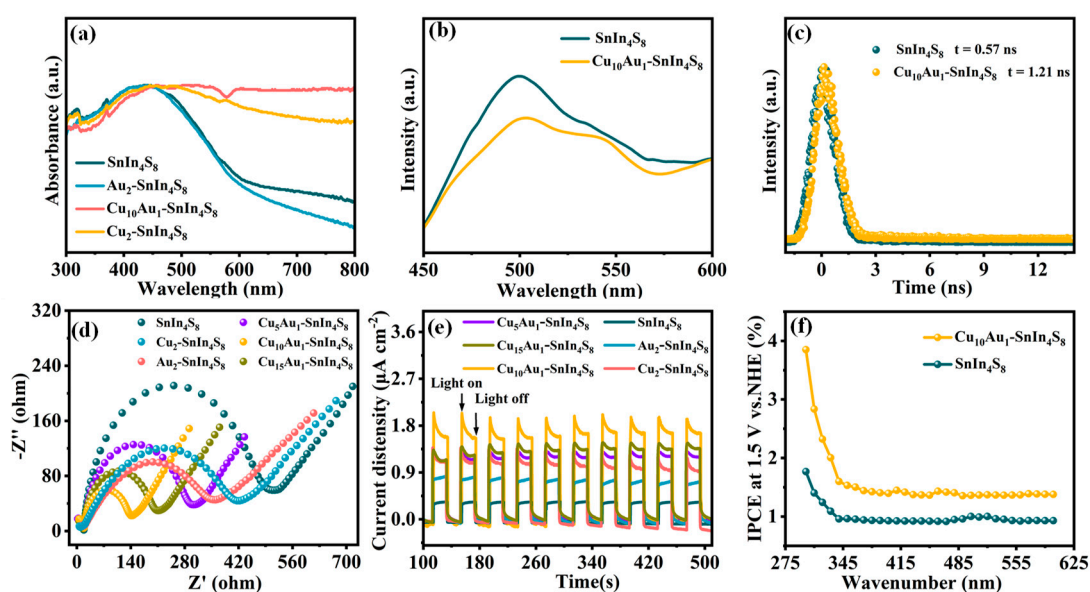


Figure 5. (a) UV-vis DRS spectra, (b) PL spectra, (c) TRPL spectra, (d) EIS and (e) transient photocurrent responses (f) IPCE of the photocatalysts.

Steady-state photoluminescence (PL) spectra are utilized to evaluate the photoexcited electrons and holes migration ability of the semiconductor photocatalyst. The decreasing PL emission intensity means a more effective inhibition of the electron-hole recombination [40]. Figure 5b shows the PL spectra of pure SnIn₄S₈ and Cu₁₀Au₁-SnIn₄S₈. The peak intensity of Cu₁₀Au₁-SnIn₄S₈ reduced remarkably as compared to SnIn₄S₈, suggesting that the loading of the CuAu alloy is able to effectively facilitate the separation and transfer of the electron-hole pairs. In addition, this enhanced charge transfer behavior was further confirmed by the time-resolved fluorescence emission decay spectra (TRPL). In Figure 5c, the average fluorescence lifetimes of Cu₁₀Au₁-SnIn₄S₈ (1.21 ns) are longer than that of pure SnIn₄S₈ (0.57 ns) because of the introduction of CuAu alloys. The extended carrier average lifetimes inevitably conduce to an accelerated separation and migration of photogenerated charge carriers, which is of great significance to promote the photoreduction CO₂ activity by offering more charge carriers to get involved in the photocatalytic process [41,42]. The above consequence was further confirmed by transient photocurrent test and electrochemical impedance spectroscopy (EIS). The different addition of metal nanocrystals on SnIn₄S₈ displayed a significant enhancement of the photocurrent intensity and decrease in the interfacial charge transfer resistances compared with the pure SnIn₄S₈, while Cu₁₀Au₁-SnIn₄S₈ possesses the smallest charge transfer resistance and the most obvious photocurrent density (Figure 5d,e). The electron trapping abilities are in the following order: SnIn₄S₈ < Au₂-SnIn₄S₈ < Cu₂-SnIn₄S₈ < Cu₅Au₁-SnIn₄S₈ < Cu₁₅Au₁-SnIn₄S₈ < Cu₁₀Au₁-SnIn₄S₈. In other words, the CuAu alloy cocatalyst is more beneficial to accelerate the photogenerated charge separation and prevent the recombination for a higher photocatalytic performance compared with the single metal cocatalyst [43]. At the same time, we carried out the incident photon-to-current conversion efficiency (IPCE) to reveal the photogenerated carrier separation and transfer efficiency (Figure 5f). Owing to the accelerated migration of photogenerated charge after Cu reacts with Au to produce the alloy, Cu₁₀Au₁-SnIn₄S₈ performs an improved IPCE from 300 to 600 nm, which greatly matches the photocatalytic activity of the samples [44].

According to the fact that the electron-hole separation was efficiently boosted significantly contributes to the photocatalytic performance, but as we all know, many factors are revealed to influence the CO₂ photoreduction activity. CO₂ capture and concentration by catalytic-active sites on the surface is another necessary factor. Hence, we used N₂ adsorption-desorption measurement to evaluate the specific surface areas of the materials. As revealed in Figure 6a, the surface areas of SnIn₄S₈, Au₂-SnIn₄S₈, Cu₂-SnIn₄S₈ and Cu₁₀Au₁-SnIn₄S₈ are, respectively, measured as 23.51, 16.35, 11.57 and 20.21 m²/g, suggesting that the load of metal nanocrystals makes an effect on the decreased specific surface area. Additionally, we conducted CO₂ adsorption tests. As displayed in Figure 6b, the Cu₁₀Au₁-SnIn₄S₈ displays the maximum CO₂ adsorption performance, which is notably higher than SnIn₄S₈. Though the surface area of Cu₁₀Au₁-SnIn₄S₈ decreases, the CO₂ adsorption capability enhances, which can be due to the synergy effect between the CuAu alloy that improves the CO₂ adsorption ability [42]. Furthermore, linear sweep voltammetry (LSV) tests are carried out to confirm the effects of the loading of the alloy on the activation ability of the CO₂ molecules. From the results revealed in Figure 6c, Cu₁₀Au₁-SnIn₄S₈ enables a clearly reduced initial potential and relatively higher current density compared with pristine SnIn₄S₈ and monometallic nanoparticles integrated into the SnIn₄S₈, which shows that the cooperative effect of the Au and Cu can remarkably facilitate the activation of CO₂ molecules and the conversion of CO₂ into hydrocarbons [45]. The above results are coupled with the increased photocatalytic CO₂ reduction performance.

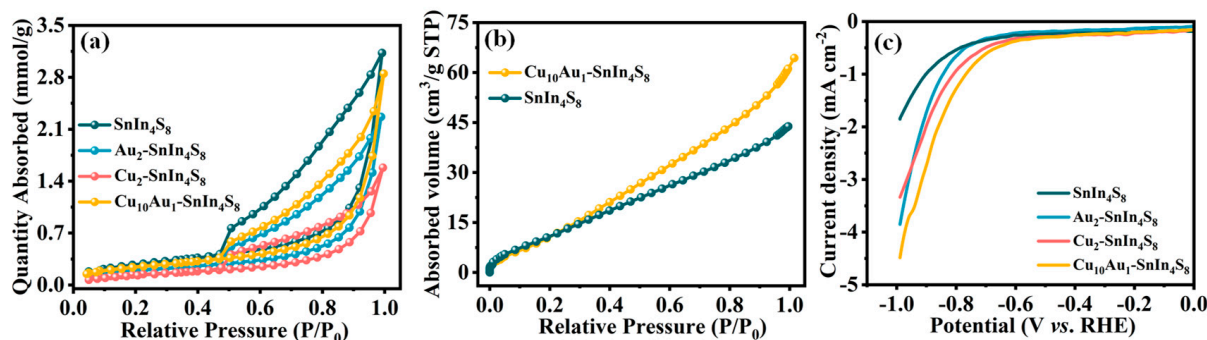


Figure 6. (a) N_2 adsorption–desorption isotherms of the samples, (b) CO_2 adsorption isotherms of SnIn_4S_8 and $\text{Cu}_{10}\text{Au}_1\text{-SnIn}_4\text{S}_8$, (c) LSV curves tested in CO_2 of the samples.

For the purpose of gaining deeper insight into the process of photocatalytic CO_2 reduction experiment, in situ Fourier transform infrared spectroscopy (in situ FTIR) experiments were utilized to investigate the key reaction intermediations. The in situ FTIR spectra of SnIn_4S_8 and $\text{Cu}_{10}\text{Au}_1\text{-SnIn}_4\text{S}_8$ were collected when filled with CO_2 gas in dark and under light irradiation for 10 min, 20 min and 30 min. By comparison (Figure 7a,b), the in situ FT-IR spectra of SnIn_4S_8 and $\text{Cu}_{10}\text{Au}_1\text{-SnIn}_4\text{S}_8$ both appear at different reaction intermediates, and two peaks located at 1213 and 1401 cm^{-1} were assigned to the bicarbonate (HCO_3^-) species, and peaks centered on 1297 cm^{-1} and 1353 cm^{-1} were attributed to the b- CO_3^{2-} and m- CO_3^{2-} . Additionally, the other two peaks detected at around 1448 cm^{-1} and 1614 cm^{-1} suggested the formation of key intermediate CO_2^- groups [37,46]. All the peaks generated in the $1000\text{--}1800$ cm^{-1} range were enhanced progressively with the extension of the UV-vis irradiation time, implying that the CO_2 absorbed on the surface of the sample can interact with photoexcited electrons to produce CO_2^- . Furthermore, CO_2^- is able to combine with H^+ to create $^*\text{COOH}$, which is the key intermediation in the process of a CO_2 conversion into CO [47]. Especially, for $\text{Cu}_{10}\text{Au}_1\text{-SnIn}_4\text{S}_8$, the tendency of the peak intensities became obviously stronger, suggesting that the loading of the CuAu alloy can strengthen the ability of the CO_2 adsorption on the photocatalyst surface and facilitate the reduction efficiency of the photocatalytic CO_2 [42].

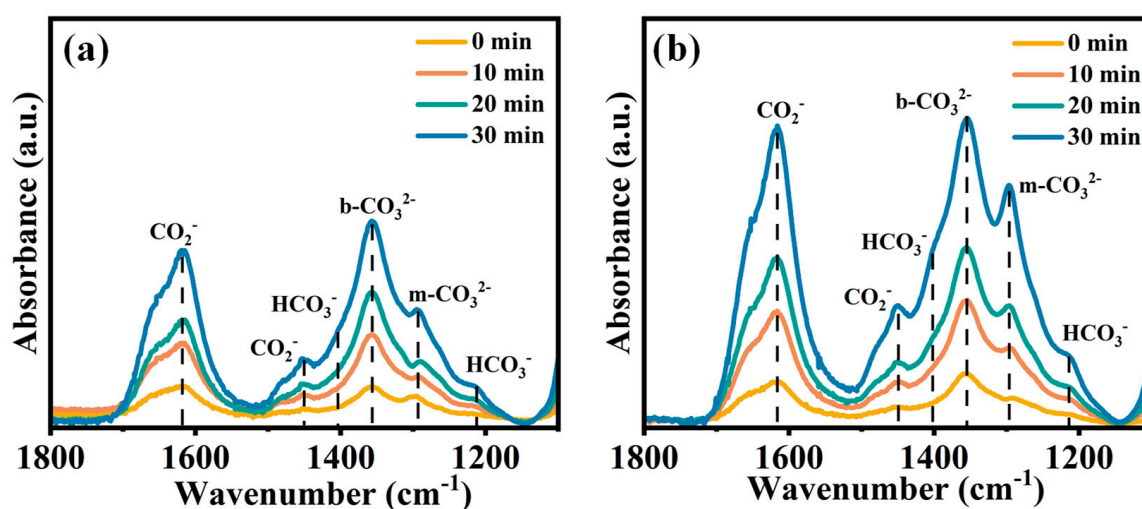
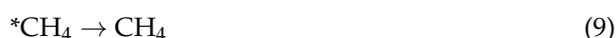
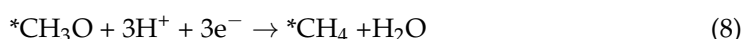
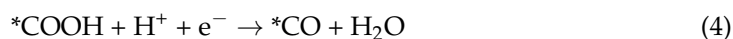
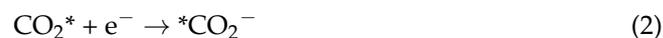


Figure 7. In situ FTIR spectra of (a) SnIn_4S_8 and (b) $\text{Cu}_{10}\text{Au}_1\text{-SnIn}_4\text{S}_8$.

The most possible CO₂ photoreduction pathways for Cu₁₀Au₁-SnIn₄S₈ can be speculated as follows:



Based on the above comprehensive experimental discussion, the possible mechanism for the photocatalytic CO₂ reduction on the CuAu-SnIn₄S₈ photocatalyst is presented in Figure 8. Under visible light irradiation, photoexcited electrons jump into the CB from the VB of SnIn₄S₈, causing many holes on the VB of SnIn₄S₈, and forming photoinduced electron-hole pairs. The photoexcited electrons then rapidly shift to the CuAu alloy nanoparticles due to their specific plasmonic property. Lastly, the electrons gather on the surface of CuAu alloys and then react with CO₂ to CO and CH₄. At the same time, the TEOA as the hole (h⁺) sacrificial agent reacts with holes in the VB of SnIn₄S₈ to further restrain the recombination of photo-induced charge carriers.

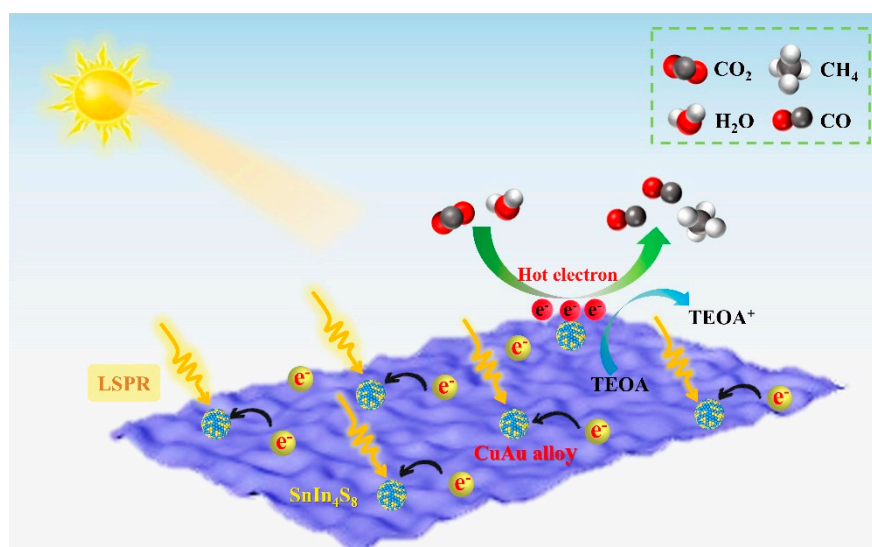


Figure 8. Schematic illustration of photocatalytic CO₂ reduction process on CuAu-SnIn₄S₈.

3. Conclusions

In summary, a novel CuAu alloy-loaded SnIn₄S₈ photocatalyst has been designed and fabricated through a facile aqueous solution method. The CuAu-SnIn₄S₈ photocatalyst displays a remarkably enhanced photocatalytic CO₂ reduction performance and stability as compared with pristine SnIn₄S₈ and single metal nanocrystals on SnIn₄S₈. The optimized performance originates from the presence of the CuAu alloy, which greatly improves the light absorption ability, acts as the synergistic site to reinforce the CO₂ adsorption and activation on the photocatalyst surface and effectively suppresses the recombination of the photoexcited charge. This work offers a useful ideal for the design of photocatalysts with

the synergistic function of the alloy cocatalysts for the high performance of a solar-driven CO₂ reduction.

Supplementary Materials: The following supporting information can be downloaded at: <https://www.mdpi.com/article/10.3390/catal12121588/s1>, Figure S1: Energy dispersive spectrometer of Cu₁₀Au₁-SnIn₄S₈; Figure S2: Survey spectra of SnIn₄S₈ and Cu₁₀Au₁-SnIn₄S₈; Figure S3: XPS valence band spectra of SnIn₄S₈ and Cu₁₀Au₁-SnIn₄S₈; Figure S4: XRD patterns of Cu₁₀Au₁-SnIn₄S₈ before and after photocatalytic CO₂ reduction reaction; Figure S5: SEM image of Cu₁₀Au₁-SnIn₄S₈ after photocatalytic CO₂ reduction reaction; Figure S6: Tauc plots of SnIn₄S₈; Figure S7: Mott-Schottky plots of SnIn₄S₈; Table S1. Comparison of the CO₂ photoreduction performance of Cu₁₀Au₁-SnIn₄S₈ catalyst with other catalysts [22,23,41,48–52].

Author Contributions: Z.Y.: writing—original draft. J.Y.: writing—review and editing. K.Y.: investigation. X.Z.: visualization. K.Z.: visualization. M.Z.: validation and formal analysis. H.J.: resources. M.H.: resources. H.L.: resources. H.X.: conceptualization, methodology, and funding acquisition. All authors have read and agreed to the published version of the manuscript.

Funding: This research was funded by the Natural Science Foundation of Jiangsu Province (BK20221367), National Natural Science Foundation of China (22075113, 22138011), High-tech Research Key Laboratory of Zhenjiang (SS2018002), Jiangsu Provincial Agricultural Science and Technology Independent Innovation Fund (CX(21)3067), Natural Science Foundation of Jiangsu Province (BK20220598).

Data Availability Statement: Data is contained within the article and Supplementary Materials.

Conflicts of Interest: The authors declare no conflict of interest.

References

1. Zu, X.; Zhao, Y.; Li, X.; Chen, R.; Shao, W.; Wang, Z.; Hu, J.; Zhu, J.; Pan, Y.; Sun, Y.; et al. Ultrastable and Efficient Visible-light-driven CO₂ Reduction Triggered by Regenerative Oxygen-Vacancies in Bi₂O₂CO₃ Nanosheets. *Angew. Chem. Int. Ed.* **2021**, *60*, 13840–13846. [[CrossRef](#)] [[PubMed](#)]
2. Li, H.; Cheng, C.; Yang, Z.; Wei, J. Encapsulated CdSe/CdS nanorods in double-shelled porous nanocomposites for efficient photocatalytic CO₂ reduction. *Nat. Commun.* **2022**, *13*, 6466. [[CrossRef](#)] [[PubMed](#)]
3. Li, P.; He, T. Recent advances in zinc chalcogenide-based nanocatalysts for photocatalytic reduction of CO₂. *J. Mater. Chem. A* **2021**, *9*, 23364–23381. [[CrossRef](#)]
4. Wang, S.; Guan, B.Y.; Lou, X.W.D. Construction of ZnIn₂S₄-In₂O₃ Hierarchical Tubular Heterostructures for Efficient CO₂ Photoreduction. *J. Am. Chem. Soc.* **2018**, *140*, 5037–5040. [[CrossRef](#)]
5. Wang, J.; Bo, T.; Shao, B.; Zhang, Y.; Jia, L.; Tan, X.; Zhou, W.; Yu, T. Effect of S vacancy in Cu₃SnS₄ on high selectivity and activity of photocatalytic CO₂ reduction. *Appl. Catal. B* **2021**, *297*, 120498. [[CrossRef](#)]
6. Yu, H.; Chen, F.; Li, X.; Huang, H.; Zhang, Q.; Su, S.; Wang, K.; Mao, E.; Mei, B.; Mul, G.; et al. Synergy of ferroelectric polarization and oxygen vacancy to promote CO₂ photoreduction. *Nat. Commun.* **2021**, *12*, 4594. [[CrossRef](#)]
7. Wang, J.; Lin, S.; Tian, N.; Ma, T.; Zhang, Y.; Huang, H. Nanostructured Metal Sulfides: Classification, Modification Strategy, and Solar-Driven CO₂ Reduction Application. *Adv. Funct. Mater.* **2020**, *31*, 2008008. [[CrossRef](#)]
8. Chandrasekaran, S.; Yao, L.; Deng, L.; Bowen, C.; Zhang, Y.; Chen, S.; Lin, Z.; Peng, F.; Zhang, P. Recent advances in metal sulfides: From controlled fabrication to electrocatalytic, photocatalytic and photoelectrochemical water splitting and beyond. *Chem. Soc. Rev.* **2019**, *48*, 4178–4280.
9. Yan, T.; Li, L.; Li, G.; Wang, Y.; Hu, W.; Guan, X. Porous SnIn₄S₈ microspheres in a new polymorph that promotes dyes degradation under visible light irradiation. *J. Hazard. Mater.* **2011**, *186*, 272–279. [[CrossRef](#)]
10. Shen, C.; Chen, Y.; Xu, X.; Li, X.; Wen, X.; Liu, Z.; Xing, R.; Guo, H.; Fei, Z. Efficient photocatalytic H₂ evolution and Cr(VI) reduction under visible light using a novel Z-scheme SnIn₄S₈/CeO₂ heterojunction photocatalysts. *J. Hazard. Mater.* **2021**, *416*, 126217. [[CrossRef](#)]
11. Chen, C.C.; Shaya, J.; Polychronopoulou, K.; Golovko, V.B.; Tesana, S.; Wang, S.Y.; Lu, C.S. Photocatalytic Degradation of Ethiofencarb by a Visible Light-Driven SnIn₄S₈ Photocatalyst. *Nanomaterials* **2021**, *11*, 1325. [[CrossRef](#)]
12. Wang, J.; Liu, M.; Wang, M.; Wang, Y.; Zhang, A.; Zhao, X.; Zeng, G.; Deng, F. Bandgap engineering of hierarchical network-like SnIn₄S₈ microspheres through preparation temperature for excellent photocatalytic performance and high stability. *Green Energy Environ.* **2019**, *4*, 264–269. [[CrossRef](#)]
13. Han, X.; Xu, D.; An, L.; Hou, C.; Li, Y.; Zhang, Q.; Wang, H. Ni-Mo nanoparticles as co-catalyst for drastically enhanced photocatalytic hydrogen production activity over g-C₃N₄. *Appl. Catal. B* **2019**, *243*, 136–144. [[CrossRef](#)]
14. Li, D.; Zhou, C.; Shi, X.; Zhang, Q.; Song, Q.; Zhou, Y.; Jiang, D. PtAg alloys as an efficient co-catalyst for CO₂ deep photoreduction with H₂O: Synergistic effects of Pt and Ag. *Appl. Surf. Sci.* **2022**, *598*, 153843. [[CrossRef](#)]

15. Jiang, D.; Zhou, Y.; Zhang, Q.; Song, Q.; Zhou, C.; Shi, X.; Li, D. Synergistic Integration of AuCu Co-Catalyst with Oxygen Vacancies on TiO₂ for Efficient Photocatalytic Conversion of CO₂ to CH₄. *ACS Appl. Mater. Interfaces* **2021**, *13*, 46772–46782. [[CrossRef](#)]
16. Zhao, L.; Ye, F.; Wang, D.; Cai, X.; Meng, C.; Xie, H.; Zhang, J.; Bai, S. Lattice Engineering on Metal Cocatalysts for Enhanced Photocatalytic Reduction of CO₂ into CH₄. *ChemSusChem* **2018**, *11*, 3524–3533. [[CrossRef](#)]
17. Li, W.; Chu, X.; Wang, F.; Dang, Y.; Liu, X.; Wang, X.; Wang, C. Enhanced cocatalyst-support interaction and promoted electron transfer of 3D porous g-C₃N₄/GO-M (Au, Pd, Pt) composite catalysts for hydrogen evolution. *Appl. Catal. B* **2021**, *288*, 120034. [[CrossRef](#)]
18. Haider, R.S.; Wang, S.; Gao, Y.; Malik, A.S.; Ta, N.; Li, H.; Zeng, B.; Dupuis, M.; Fan, F.; Li, C. Boosting photocatalytic water oxidation by surface plasmon resonance of Ag_xAu_{1-x} alloy nanoparticles. *Nano Energy* **2021**, *87*, 106189. [[CrossRef](#)]
19. Fu, S.; Zhu, C.; Shi, Q.; Xia, H.; Du, D.; Lin, Y. Highly branched PtCu bimetallic alloy nanodendrites with superior electrocatalytic activities for oxygen reduction reactions. *Nanoscale* **2016**, *8*, 5076–5081. [[CrossRef](#)]
20. Lee, S.; Jeong, S.; Kim, W.D.; Lee, S.; Lee, K.; Bae, W.K.; Moon, J.H.; Lee, S.; Lee, D.C. Low-coordinated surface atoms of CuPt alloy cocatalysts on TiO₂ for enhanced photocatalytic conversion of CO₂. *Nanoscale* **2016**, *8*, 10043–10048. [[CrossRef](#)]
21. Yu, Y.; Dong, X.; Chen, P.; Geng, Q.; Wang, H.; Li, J.; Zhou, Y.; Dong, F. Synergistic Effect of Cu Single Atoms and Au-Cu Alloy Nanoparticles on TiO₂ for Efficient CO₂ Photoreduction. *ACS Nano* **2021**, *15*, 14453–14464. [[CrossRef](#)] [[PubMed](#)]
22. Liu, Q.; Chen, Q.; Li, T.; Ren, Q.; Zhong, S.; Zhao, Y.; Bai, S. Vacancy engineering of AuCu cocatalysts for improving the photocatalytic conversion of CO₂ to CH₄. *J. Mater. Chem. A* **2019**, *7*, 27007–27015. [[CrossRef](#)]
23. Wang, Z.; Lee, H.; Chen, J.; Wu, M.; Leung, D.Y.C.; Grimes, C.A.; Lu, Z.; Xu, Z.; Feng, S.-P. Synergistic effects of Pd-Ag bimetals and g-C₃N₄ photocatalysts for selective and efficient conversion of gaseous CO₂. *J. Power Sources* **2020**, *466*, 228306. [[CrossRef](#)]
24. Jia, X.; Zhao, J.; Lv, Y.; Fu, X.; Jian, Y.; Zhang, W.; Wang, Y.; Sun, H.; Wang, X.; Long, J.; et al. Low-crystalline PdCu alloy on large-area ultrathin 2D carbon nitride nanosheets for efficient photocatalytic Suzuki coupling. *Appl. Catal. B* **2022**, *300*, 120756. [[CrossRef](#)]
25. Cai, X.; Wang, A.; Wang, J.; Wang, R.; Zhong, S.; Zhao, Y.; Wu, L.; Chen, J.; Bai, S. Order engineering on the lattice of intermetallic PdCu co-catalysts for boosting the photocatalytic conversion of CO₂ into CH₄. *J. Mater. Chem. A* **2018**, *6*, 17444–17456. [[CrossRef](#)]
26. Long, R.; Li, Y.; Liu, Y.; Chen, S.; Zheng, X.; Gao, C.; He, C.; Chen, N.; Qi, Z.; Song, L.; et al. Isolation of Cu Atoms in Pd Lattice: Forming Highly Selective Sites for Photocatalytic Conversion of CO₂ to CH₄. *J. Am. Chem. Soc.* **2017**, *139*, 4486–4492. [[CrossRef](#)]
27. Bhunia, K.; Chandra, M.; Khilari, S.; Pradhan, D. Bimetallic PtAu Alloy Nanoparticles-Integrated g-C₃N₄ Hybrid as an Efficient Photocatalyst for Water-to-Hydrogen Conversion. *ACS Appl. Mater. Interfaces* **2019**, *11*, 478–488. [[CrossRef](#)]
28. Yan, P.C.; Jin, Y.C.; Xu, L.; Mo, Z.; Qian, J.C.; Chen, F.; Yuan, J.J.; Xu, H.; Li, H.N. Enhanced photoelectrochemical aptasensing triggered by nitrogen deficiency and cyano group simultaneously engineered 2D carbon nitride for sensitively monitoring atrazine. *Biosens. Bioelectron.* **2022**, *206*, 114144. [[CrossRef](#)]
29. Liu, H.; Li, M.; Dao, T.D.; Liu, Y.; Zhou, W.; Liu, L.; Meng, X.; Nagao, T.; Ye, J. Design of PdAu alloy plasmonic nanoparticles for improved catalytic performance in CO₂ reduction with visible light irradiation. *Nano Energy* **2016**, *26*, 398–404. [[CrossRef](#)]
30. Shi, L.Z.; Liu, H.M.; Ning, S.B.; Ye, J.H. Localized surface plasmon resonance effect enhanced Cu/TiO₂ core-shell catalyst for boosting CO₂ hydrogenation reaction. *Catal. Sci. Technol.* **2022**, *12*, 6155–6162. [[CrossRef](#)]
31. Liu, H.; Meng, X.; Dao, T.D.; Zhang, H.; Li, P.; Chang, K.; Wang, T.; Li, M.; Nagao, T.; Ye, J. Conversion of Carbon Dioxide by Methane Reforming under Visible-Light Irradiation: Surface-Plasmon-Mediated Nonpolar Molecule Activation. *Angew. Chem. Int. Ed. Engl.* **2015**, *54*, 11545–11549. [[CrossRef](#)] [[PubMed](#)]
32. Pan, B.; Wu, Y.; Rhimi, B.; Qin, J.; Huang, Y.; Yuan, M.; Wang, C. Oxygen-doping of ZnIn₂S₄ nanosheets towards boosted photocatalytic CO₂ reduction. *J. Energy Chem.* **2021**, *57*, 1–9. [[CrossRef](#)]
33. Lang, Q.; Yang, Y.; Zhu, Y.; Hu, W.; Jiang, W.; Zhong, S.; Gong, P.; Teng, B.; Zhao, L.; Bai, S. High-index facet engineering of PtCu cocatalysts for superior photocatalytic reduction of CO₂ to CH₄. *J. Mater. Chem. A* **2017**, *5*, 6686–6694. [[CrossRef](#)]
34. Cai, X.; Wang, F.; Wang, R.; Xi, Y.; Wang, A.; Wang, J.; Teng, B.; Bai, S. Synergism of surface strain and interfacial polarization on Pd@Au core-shell cocatalysts for highly efficient photocatalytic CO₂ reduction over TiO₂. *J. Mater. Chem. A* **2020**, *8*, 7350–7359. [[CrossRef](#)]
35. Jiao, J.; Wei, Y.; Zhao, Y.; Zhao, Z.; Duan, A.; Liu, J.; Pang, Y.; Li, J.; Jiang, G.; Wang, Y. AuPd/3DOM-TiO₂ catalysts for photocatalytic reduction of CO₂: High efficient separation of photogenerated charge carriers. *Appl. Catal. B* **2017**, *209*, 228–239. [[CrossRef](#)]
36. Mo, Z.; Wu, G.; Yan, P.; Zhu, X.; Qian, J.; Lei, Y.; Xu, L.; Xu, H.; Li, H. Engineering oxygen into ultrathin graphitic carbon nitride: Synergistic improvement of electron reduction and charge carrier dynamics for efficient photocatalysis. *Mater. Today Chem.* **2022**, *25*, 100956. [[CrossRef](#)]
37. Li, X.; Jiang, H.P.; Ma, C.C.; Zhu, Z.; Song, X.H.; Li, X.Y.; Wang, H.Q.; Huo, P.W.; Chen, X.B. Construction of a multi-interfacial-electron transfer scheme for efficient CO₂ photoreduction: A case study using CdIn₂S₄ micro-flower spheres modified with Au nanoparticles and reduced graphene oxide. *J. Mater. Chem. A* **2020**, *8*, 18707–18714. [[CrossRef](#)]
38. Tian, J.; Zhong, K.; Zhu, X.; Yang, J.; Mo, Z.; Liu, J.; Dai, J.; She, Y.; Song, Y.; Li, H.; et al. Highly exposed active sites of Au nanoclusters for photocatalytic CO₂ reduction. *Chem. Eng. J.* **2023**, *451*, 138392.
39. Han, D.; Bao, Z.; Xing, H.; Yang, Y.; Ren, Q.; Zhang, Z. Fabrication of plasmonic Au-Pd alloy nanoparticles for photocatalytic Suzuki-Miyaura reactions under ambient conditions. *Nanoscale* **2017**, *9*, 6026–6032. [[CrossRef](#)]

40. Yang, J.; Zhu, X.; Yu, Q.; Zhou, G.; Li, Q.; Wang, C.; Hua, Y.; She, Y.; Xu, H.; Li, H. Plasma-induced defect engineering: Boosted the reverse water gas shift reaction performance with electron trap. *J. Colloid Interface Sci.* **2020**, *580*, 814–821. [[CrossRef](#)]
41. Yang, J.; Zhu, X.; Yu, Q.; He, M.; Zhang, W.; Mo, Z.; Yuan, J.; She, Y.; Xu, H.; Li, H. Multidimensional In₂O₃/In₂S₃ heterojunction with lattice distortion for CO₂ photoconversion. *Chin. J. Catal.* **2022**, *43*, 1286–1294. [[CrossRef](#)]
42. Yang, J.; Jing, L.; Zhu, X.; Zhang, W.; Deng, J.; She, Y.; Nie, K.; Wei, Y.; Li, H.; Xu, H. Modulating electronic structure of lattice O-modified orange polymeric carbon nitrogen to promote photocatalytic CO₂ conversion. *Appl. Catal. B* **2023**, *320*, 122005. [[CrossRef](#)]
43. Huang, J.; Mensi, M.; Oveisi, E.; Mantella, V.; Buonsanti, R. Structural Sensitivities in Bimetallic Catalysts for Electrochemical CO₂ Reduction Revealed by Ag-Cu Nanodimers. *J. Am. Chem. Soc.* **2019**, *141*, 2490–2499. [[CrossRef](#)]
44. Yang, Z.; Yang, J.; Ji, H.; He, M.; Song, Y.; Zhang, W.; Yuan, J.; She, X.; She, Y.; Li, H.; et al. Construction of S-Co-S internal electron transport bridges in Co-doped CuInS₂ for enhancing photocatalytic CO₂ reduction. *Mater. Today Chem.* **2022**, *26*, 101078. [[CrossRef](#)]
45. Qiu, B.; Huang, P.; Lian, C.; Ma, Y.; Xing, M.; Liu, H.; Zhang, J. Realization of all-in-one hydrogen-evolving photocatalysts via selective atomic substitution. *Appl. Catal. B* **2021**, *298*, 120518. [[CrossRef](#)]
46. Li, X.D.; Sun, Y.F.; Xu, J.Q.; Shao, Y.J.; Wu, J.; Xu, X.L.; Pan, Y.; Ju, H.X.; Zhu, J.F.; Xie, Y. Selective visible-light-driven photocatalytic CO₂ reduction to CH₄ mediated by atomically thin CuIn₅S₈ layers. *Nat. Energy* **2019**, *4*, 690–699. [[CrossRef](#)]
47. Zhu, X.; Yang, J.; Zhu, X.; Yuan, J.; Zhou, M.; She, X.; Yu, Q.; Song, Y.; She, Y.; Hua, Y.; et al. Exploring deep effects of atomic vacancies on activating CO₂ photoreduction via rationally designing indium oxide photocatalysts. *Chem. Eng. J.* **2021**, *422*, 129888. [[CrossRef](#)]
48. Yang, J.; Zhu, X.; Mo, Z.; Yi, J.; Yan, J.; Deng, J.; Xu, Y.; She, Y.; Qian, J.; Xu, H.; et al. A multidimensional In₂S₃-CuInS₂ heterostructure for photocatalytic carbon dioxide reduction. *Inorg. Chem. Front.* **2018**, *5*, 3163–3169.
49. Zhang, Z.; Cao, Y.; Zhang, F.; Li, W.; Li, Y.; Yu, H.; Wang, M.; Yu, H. Tungsten oxide quantum dots deposited onto ultrathin CdIn₂S₄ nanosheets for efficient S-scheme photocatalytic CO₂ reduction via cascade charge transfer. *Chem. Eng. J.* **2022**, *428*, 131218. [[CrossRef](#)]
50. Han, Q.; Li, L.; Gao, W.; Shen, Y.; Wang, L.; Zhang, Y.; Wang, X.; Shen, Q.; Xiong, Y.; Zhou, Y.; et al. Elegant Construction of ZnIn₂S₄/BiVO₄ Hierarchical Heterostructures as Direct Z-Scheme Photocatalysts for Efficient CO₂ Photoreduction. *ACS Appl. Mater. Interfaces* **2021**, *13*, 15092–15100. [[CrossRef](#)]
51. Xia, Y.; Cheng, B.; Fan, J.; Yu, J.; Liu, G. Near-infrared absorbing 2D/3D ZnIn₂S₄/N-doped graphene photocatalyst for highly efficient CO₂ capture and photocatalytic reduction. *Sci. China Mater.* **2020**, *63*, 552–565. [[CrossRef](#)]
52. Ye, W.; Hu, J.; Hu, X.; Zhang, W.; Ma, X.; Wang, H. Rational Construction of Z-Scheme CuInS₂/Au/g-C₃N₄ Heterostructure: Experimental Results and Theoretical Calculation. *ChemCatChem* **2019**, *11*, 6372–6383. [[CrossRef](#)]